

Swarthmore College

Works

Senior Theses, Projects, and Awards

Student Scholarship

Spring 2019

Monitoring Silver Nanoparticle Aggregation In situ by Integrating Particle Impact Voltammetry and UV-Vis Spectroscopy

Laela Ezra , '19

Follow this and additional works at: <https://works.swarthmore.edu/theses>

 Part of the [Chemistry Commons](#)

Recommended Citation

Ezra, Laela , '19, "Monitoring Silver Nanoparticle Aggregation In situ by Integrating Particle Impact Voltammetry and UV-Vis Spectroscopy" (2019). *Senior Theses, Projects, and Awards*. 237.
<https://works.swarthmore.edu/theses/237>

Please note: the theses in this collection are undergraduate senior theses completed by senior undergraduate students who have received a bachelor's degree.

This work is brought to you for free by Swarthmore College Libraries' Works. It has been accepted for inclusion in Senior Theses, Projects, and Awards by an authorized administrator of Works. For more information, please contact myworks@swarthmore.edu.

Monitoring Silver Nanoparticle Aggregation *In situ* by Integrating Particle Impact Voltammetry and UV- Vis Spectroscopy

Presented as a Senior Course Thesis in Chemistry

Laela Ezra
May 13th, 2019
Swarthmore College

Advisor: Kathryn R. Riley

Table of Contents

| | |
|---|----|
| List of Common Abbreviations | 3 |
| List of Figures and Tables | 4 |
| Abstract | 6 |
| Chapter 1: Introduction | 7 |
| 1.1 Silver Nanoparticles and their Properties | 7 |
| 1.2 Aggregation of AgNPs | 9 |
| 1.3 Survey of AgNP Characterization Techniques | 12 |
| 1.4 Particle Impact Voltammetry (PIV) | 14 |
| 1.5 UV-Vis Spectroscopy | 16 |
| 1.6 Research Aims | 17 |
| Chapter 2: Materials and Methods | 18 |
| 2.1 Chemicals | 18 |
| 2.2 AgNP Size Characterization by DLS and SEM | 18 |
| 2.3 UV-Vis Parameters | 19 |
| 2.4 Electrochemistry Parameters | 19 |
| Chapter 3: Characterization of AgNPs | 21 |
| 3.1 Characterization by DLS and SEM | 21 |
| 3.2 Characterization by UV-Vis Spectroscopy | 22 |
| 3.3 Electrochemical characterization | 24 |
| Chapter 4: Merging Techniques | 29 |
| 4.1 Development of hybrid cell | 29 |
| 4.2 Proof-of-Principle Aggregation Experiments | 31 |
| 4.3 Optimizing the Performance of the Integrated PIV and UV-Vis Technology for Monitoring AgNP Aggregation | 33 |
| Chapter 5: Conclusions and Future Directions | 39 |
| Acknowledgements | 41 |
| Appendix | 42 |
| References | 46 |

List of Common Abbreviations

AF4—Asymmetric flow field flow fractionation
AgNP—Silver nanoparticle
CCC—Critical coagulation concentration
CE—Capillary electrophoresis
CV—Cyclic voltammogram
 d_{AgNP} —Silver nanoparticle diameter
DLS—Dynamic light scattering
ENM—Engineered nanomaterial
ICP-MS—Inductively coupled plasma mass spectrometry
 k_{agg} —Rate constant of aggregation
 λ_{max} —Maximum absorbance wavelength
LSPR—Local surface plasmon resonance
PC—Polycarbonate
PDI—Polydispersity index
PIV—Particle impact voltammetry
SEM—Scanning electron microscopy
TEM—Tunneling electron microscopy
UME—Ultramicroelectrode

List of Figures and Tables

| | |
|---|----|
| Figure 1. Illustration of a nanoparticle, nanorod, and nanoplate..... | 7 |
| Figure 2. AgNP solutions increasing in size from 10 nm to 200 nm (left to right)..... | 16 |
| Figure 3. (A) UV-Vis spectra for 10, 20, 40, and 80 nm AgNPs and (B) Offset kinetics data for 10, 20, and 40 nm AgNPs | 23 |
| Figure 4. Representative kinetics curves at various concentrations of NaCl (A) before and (B) after optimization attempts | 24 |
| Figure 5. Number of transients obtained for several 1-minute scans of AgNPs as a function of pH at a potential of (A) + 0.3 V and (B) +0.5 V | 24 |
| Figure 6. Sample amperometric curves for 10, 20, 40, and 80 nm AgNPs, offset for clarity | 26 |
| Figure 7. Faradaic Curves obtained for (A) 10 nm, (B) 20 nm, (C) 40 nm, and (D) 80 nm AgNPs..... | 28 |
| Figure 8. Image and diagram depicting spectroelectrochemical cell | 29 |
| Figure 9. Printed-polycarbonate caps before and after extended submersion in dilute (~5%) nitric acid..... | 30 |
| Figure 10. 3D digital models for the spectroelectrochemical cap | 31 |
| Figure 11. (A) Absorbance scans of AgNPs in UV-Vis only spectrometer and hybrid cell setup. (B) Amperometric curves of PIV only cell and hybrid cell setup..... | 32 |
| Figure 12. Sample collection of PIV, UV-Vis spectra, and kinetics. | 33 |
| Figure 13. Two replicates of data collected from a 30-minute aggregation study with NanoXact 40 nm particles in 40 mM NaCl 10 mM citrate solution: (A) size of AgNPs as determined by PIV, (B) UV-Vis spectra obtained at each interval, and (C) kinetics data at the lambda max | 34 |
| Figure 14. Representative data of 40 nm particles in (A-B) 20 mM and (C-D) 40 mM NaCl solution | 35 |
| Figure 15. (A) Initial UV-Vis kinetics data and (B) kinetics constants obtained for 40 nm AgNP aggregation experiments in 20 and 40 mM NaCl, 10 mM citrate buffer. $\lambda_{\max} = 410$ nm..... | 36 |
| Figure 16. (A) Transients per replicate at different NaCl concentrations and (B) k values from kinetic fitting..... | 38 |
| Table 1. Average AgNP diameters and standard deviation as obtained through DLS zeta potential measurements and SEM images | 22 |
| Table 2. Linear fit parameters for 40 nm AgNP kinetic data in various NaCl concentrations | 37 |
| Table 3. Average particle diameters of 40 nm AgNPs after exposure to salt buffers | 37 |

| | |
|--|----|
| Figure A 1. Representative SEM images for AgNP lots | 43 |
| Table A1. AgNP lots ordered from NanoComposix..... | 42 |
| Table A2. Exponential decay fit parameters for 40 nm AgNP kinetic data in various NaCl concentrations | 44 |
| Table A3. First-order fit parameters for 40 nm AgNP kinetic data in various NaCl concentrations | 45 |

Abstract

Engineered nanomaterials (ENMs) have been increasingly used for a variety of purposes. Silver nanoparticles (AgNPs) are the most widely-used ENM to date. AgNPs undergo many transformations while in solution and in biologically relevant environments, so the development of techniques to analyze the extent of these transformations is crucial. The transformation of interest for this work is AgNP aggregation.

There exist techniques to monitor aggregation of AgNPs and other ENMs (such as scanning electron microscopy) but often these instruments cannot measure aggregation *in situ*: some cannot monitor aggregation in real-time, and none are suited for fieldwork. Two methods that can characterize AgNP aggregation are particle impact voltammetry (PIV) and UV-Vis spectroscopy. PIV measures the number of electrons transferred by oxidation of an AgNP, providing particle-specific size data. Supplementing this data, UV-Vis data provides information about the bulk AgNP suspension by measuring local surface plasmon resonance (LSPR). Both are relatively inexpensive and transportable methods and thus were selected to be incorporated.

These methods were first individually used to characterize AgNP size and population, which was confirmed with dynamic light scattering (DLS) and SEM data. After initial optimization of these methods, a hybrid cell was designed such that PIV and UV-Vis data could be collected simultaneously. This involved creation of a specialized cap and optimization of the collection methods.

A sample study was performed to test how the integrated method measured aggregation. Aggregation of AgNPs was induced by increasing electrolyte concentration. Simultaneous collection of PIV and UV-Vis spectra and kinetics data was performed. The spectral data and kinetics data were consistent with expected aggregation trends, while PIV data initially did not show a clear relationship between measured AgNP size and electrolyte concentration. Upon further investigation of the PIV data, a relationship between transient frequency and aggregation rate constants was found. More studies are needed to investigate this further.

Chapter 1: Introduction

Engineered nanomaterials (ENMs) have become more prevalently used in everyday consumer products due to their unique properties. However, ENMs can undergo a number of transformations as they encounter biological and environmental matrices. The increased use of ENMs and the complexity of their transformations necessitate the development of new analytical techniques to study their properties *in situ*. In this work, a new technique that couples UV-Vis spectroscopy with an advanced electrochemistry technique, particle impact voltammetry (PIV), was developed to probe the aggregation of silver nanoparticles (AgNPs) *in situ*. Herein, the motivation for developing this technique, as well as development, validation, and application of the technique are described.

1.1 Silver Nanoparticles and their Properties

ENMs are materials that are precisely designed to have one or more dimensions below 100 nm.¹ They have a variety of shapes, including nanoparticles (three nanoscale dimensions), nanorods (two nanoscale dimensions), and nanoplates (one nanoscale dimension) (**Figure 1**. Illustration of a nanoparticle, nanorod, and nanoplate. Nanoscale dimensions are marked by white arrows.). They also have a variety of compositions, including metal (e.g., Ag, Au, Zn, Fe), metal oxide (e.g., TiO₂, ZnO), organic (e.g., C, polystyrene, silica), and a variety of composites (e.g., Ag-shelled Au, Au-shelled silica). At the nanoscale, quantum effects dominate the behavior of the particles, such that the ENMs have

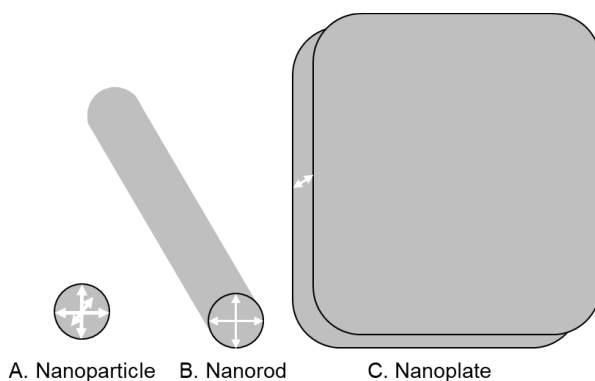


Figure 1. Illustration of a nanoparticle, nanorod, and nanoplate. Nanoscale dimensions are marked by white arrows.

many unique properties compared to the corresponding bulk-scale material.² These properties, such as optical properties, electrical conductivity, and reactivity, can be tuned by changing the size, shape, and composition of the ENMs. For example, while bulk-scale silver is characterized as a grayish metal, a solution of silver nanoparticles (AgNPs) is yellow, or a solution of silver nanoplates can be blue or green depending on the size. The tunability of ENM properties has enabled their use in a variety of fields, including energy technologies, chemical catalysis, electronics, medicine, and consumer products.^{1,3}

As of 2014, nano-enabled products represented greater than a \$1 trillion industry.⁴ Of this market, silver nanoparticles constitute approximately 25% and are produced at a rate of about 500 tons per year.⁵ Thus, they represent an ENM of significant economic importance. AgNPs are used widely in medicine and food packaging due to their antimicrobial properties. This is primarily due to the effectiveness of Ag(I) at inhibiting microbial growth. AgNPs can undergo oxidative dissolution to release Ag(I) ions, according to: $2Ag(s) + \frac{1}{2}O_2(aq) + 2H^+(aq) \rightarrow 2Ag(I)(aq) + H_2O(l)$. Ag(I) can inhibit protein function and DNA replication and interfere with the electron transport chain. It can also lead to the production of reactive oxygen species.^{6,7} These cytotoxic properties make AgNPs useful for a variety of medical applications, including wound dressings, cleaning solutions for surgical tools, and as coatings in medical devices (e.g., catheters). Composite nanomaterials that contain silver (such as graphene-silver/graphene-silver oxide) also release Ag(I) and exhibit similar antimicrobial effects.⁸ The release of Ag(I) and/or AgNPs from these products depends on how the particles are incorporated into the product, as well as the product's end-use.³ For example, exposure to

artificial sweat resulted in the highest leaching of Ag(I) when compared to distilled water and tap water.³

1.2 Aggregation of AgNPs

AgNPs can undergo several different transformations in solution. These transformations can occur simultaneously and are important to understanding how these ENMs behave *in situ*. Examples of these transformations include oxidation and sulfidation, adsorption of natural organic matter (NOM), and formation of a protein corona. Though all transformations are important to consider when developing an analytical method, of these transformations, the one most relevant to this work is aggregation.

AgNPs are one of several ENMs that exhibit aggregation properties. Perturbation of the AgNP suspension leads to favorable inter-particle interactions and formation of polymers. Similar to aggregation, agglomeration is a phenomenon that is observed for AgNPs. Unlike aggregates, however, AgNP agglomerates can be restored to the monomeric form by sonication or purging with nitrogen gas.⁹

Derjaguin-Landau-Verwey-Overbeek (DLVO) theories provide a fairly extensive description of nanoparticle aggregation. Aggregation is a set of fractal processes, described by the relation:

$$m(R) \propto a_h^{d_F} \quad (1)$$

where $m(R)$ is aggregate mass, a_h is the aggregate's hydrodynamic radius and d_F is the fractal dimension, or how compactly arranged the particles are in the aggregate.¹⁰ From this main relation, rate equations for aggregation can be formulated, accounting for

attractive forces and van der Waals forces between a pair of nanoparticles.¹⁰ The relevant rate equation that models monodisperse particles of the same diameter is:

$$\frac{dn_k}{dt} = -\frac{4}{3}\alpha\frac{k_B T}{\mu}n_i^2 \quad (2)$$

where n_i is the number concentration of aggregates comprised of i number primary particles, α is the collision efficiency function, and μ is viscosity of solution (0.001 Pa·s).¹⁰

Due to the initial prominence of dimerization over other types of polymer formation, early aggregation can be modeled by a second order rate equation:

$$\left(\frac{dn_1}{dt}\right)_{t \rightarrow 0} = -k_{11}n_0^2 \quad (3)$$

where n_1 is monomeric particle concentration, k_{11} is an absolute rate constant for two identical particles, and n_0 is the initial monomeric particle concentration.¹⁰ This second-order relationship can be a useful starting point when analyzing bulk colloidal data from UV-Vis spectroscopy, as described later in this work. Two regimes are then derived from this basic tenement of DLVO theory: diffusion-limited colloidal aggregation (DLCA) and reaction-limited colloidal aggregation (RLCA). These are differentiated by a collision efficiency value ranging from 0 to 1 (1 is 100% collision efficiency); the collision efficiency for RLCA >1 and near 1 for DLCA.¹⁰ If the barrier to aggregation is not overcome by reaction conditions, (*e.g.*, pH, ion concentration), then RLCA dominates.¹¹

While DLVO theory is pivotal in forming most aggregation models, it is not a perfect method. One limit of classic DLVO theory is the assumption that aggregation depends primarily on electrostatic forces. This is true at certain distances between two given particles, but other surficial forces are in effect, such as hydration forces, osmotic attraction, steric/entropic repulsions, and others.¹⁰ Extended DLVO theory accounts for

forces that classical DLVO misses (ex. Lewis acid-base interactions). This tends to increase the complexity of the models, but is needed to apply the theory generally.¹⁰

Another limit of classical DLVO is that the particle model is spherical. This does not account for how aggregation forces act differently on nanorods and nanoplates, so other theories like surface element integration must be taken into consideration for modeling non-spherical particles.¹⁰ Surface coatings affect aggregation significantly: they can introduce additional steric, electrostatic, or electrosteric repulsions.¹⁰ For example, two common AgNP coatings that utilize electrostatic and steric forces respectively are citrate and polyvinylpyrrolidone (PVP). Classical DLVO theory models coatings that rely on electrostatics well, but again does not account for other forces.

Varying the pH and electrolyte concentration affects the nanoparticle's surface charge. AgNPs are often capped with negatively charged molecules like citrate, which provide colloidal stabilization via electrostatic repulsion between neighboring AgNPs. The addition of ions to solution disrupts the charge layer, allowing for AgNPs to agglomerate and aggregate. High ionic concentrations result in quicker aggregation times, and the critical coagulation concentration (CCC) defines where aggregation occurs most readily.¹⁰ DLCA occurs once the CCC for a particular colloid is reached, while RLCA occurs at concentrations lesser than the CCC.¹²

The introduction of light and oxygen are known to affect aggregation as well.^{7,13,14} Over approximately 4 to 6 hours, the presence of dissolved oxygen has been shown to oxidize AgNPs to Ag(I), which can adsorb to other surfaces or form precipitates with other ions in solution (*e.g.*, chloride).^{13,15} When examining a method to quantify aggregation, it is important to control these factors as well.

1.3 Survey of AgNP Characterization Techniques

While AgNPs and other ENMs have potential for a variety of applications, it is crucial to understand how these technologies behave after they have been used. There is a need to develop methods that can quantify how intended and unintended contact with ENMs may affect humans and the environment. Some methods for AgNP characterization include: transmission electron microscopy and scanning electron microscopy (TEM and SEM), capillary electrophoresis (CE) and inductively coupled plasma mass spectrometry (ICP-MS)¹⁶, UV-Vis spectroscopy, differential centrifugal sedimentation (DCS), asymmetric flow field flow-fractionation (AF4)^{17,18}, nanoparticle tracking analysis (NTA)¹⁹, and dynamic light scattering (DLS). These methods of ENM characterization can be grouped by their primary method of data collection: image analysis, population separation, and optical perturbation.

Microscopy techniques constitute much of the image analysis category. SEM and TEM generate 2D images that indicate particle shape, size, and coatings/coronas. These techniques can clearly demonstrate what types of transformations may have taken place. TEM and SEM images are often used as standards for other methods, for example to confirm size distributions or to confirm that transformations have taken place. A weakness of SEM is sample preparation: ENMs must be prepared on dried wafers; *in situ* measurements are not typically performed with this type of microscopy. A modification of TEM known as environmental TEM (ETEM) enables *in situ* measurement of nanoparticles, but real-time aggregation data cannot be obtained through this method.^{20,21}

CE is one of many separation techniques that have been applied for the analysis of nanomaterials. CE separates analytes based on their electrophoretic mobility, which is a function of both the analyte charge and the analyte size. This technique can be coupled

with others to obtain more information about ENMs. Qu et al. applied CE coupled with single-particle ICP-MS to analyze gold nanoparticles in dietary supplements.¹⁶ Using CE, AuNPs of varying diameter were separated and elemental analysis using single particle ICP-MS enabled determination of nanoparticle diameters from eluted CE fractions. These diameters were found to be comparable to diameters determined by TEM.¹⁶ The use of CE alone enables separation of particles, but not confirmation of particle size. ICP-MS alone is unable to physically separate particles of varying size but allows for determination of size distributions. The combined CE-ICP-MS technique accounts for the flaws in each individual technique. Another study combined CE with DCS to determine mass concentrations of particle mixtures, but while this was feasible, the concentrations were only relative and required significant knowledge of instrument and experiment parameters.²² Relative concentrations are still helpful in the detection of agglomerated particles.

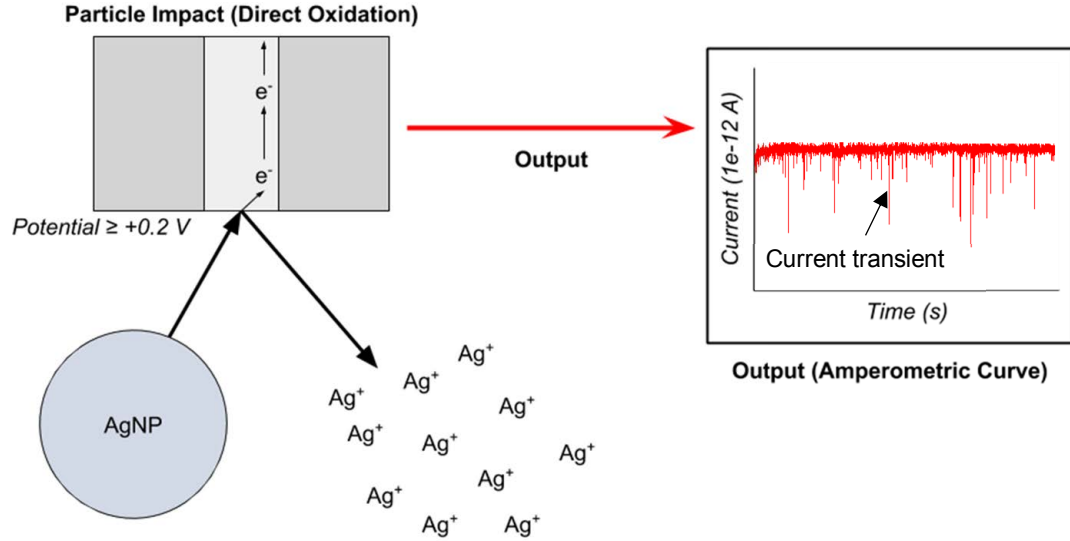
Like CE, AF4 is another separation technique that can be applied to ENMs. It utilizes the differences in the coefficients of diffusion to separate ENMs.²³ First, an aqueous solution of ENMs flows through a channel, concentrating near an injection port. This is known as the focusing step. Once properly focused, separation occurs: an applied flow first pushes all nanoparticles to a membrane, and then due to Brownian motion, the particles travel away from the membrane to elute from the channel. Particles with the smallest size (and thus larger diffusion coefficient) elute first. AF4 is relatively straightforward and it is easy to separate nanoparticle populations, but since it uses a membrane in its channel, particle loss and variability in retention time can occur due to particle-membrane interactions.¹⁸

UV-Vis and DLS both rely on differing optical qualities to characterize ENMs. These techniques are also often used in conjunction with other techniques as auxiliary measurements. DLS, however, provides size distributions of nanoparticles skewed to larger nanoparticles while UV-Vis only indicates presence of monomeric nanoparticles.^{24,25} One study by Lodeiro et al. is an exception to using UV-Vis in an auxiliary fashion; their primary method of quantifying AgNP aggregation was through UV-Vis.²⁶

1.4 Particle Impact Voltammetry (PIV)

One of the less established techniques that has the potential to characterize ENMs at the nanoscale is that of anodic particle coulometry, or particle-impact voltammetry (PIV). PIV is an electrochemical technique capable of detecting single nanoparticle redox events. There are three primary modes for carrying out PIV experiments: (1) direct reduction or oxidation of the ENM, (2) blocking of a redox cycling reaction by an ENM, or (3) catalysis of a redox reaction by an ENM.²⁷ Silver has distinct redox capabilities, which enables the use of PIV in direct oxidation mode.

First, a microelectrode or ultramicroelectrode (UME) is held at a constant potential. An UME is preferable because the smaller surface area reduces background current and the chance that multiple redox events occur concurrently, thus reducing noise and difficulty in signal interpretation. The AgNPs diffuse under Brownian motion to the UME, where they are oxidized at the UME surface. This results in a flux of electrons transferred at the UME surface and a measurable change in current, also known as a current transient (**Scheme 1**).²⁸ Current transients appear as sharp, spike-like peaks as opposed to a staircase response. This is because the contact time between an AgNP and the electrode is not long relative to the collection time.^{28,29}



Scheme 1. Particle impact voltammetry via direct oxidation. Potential at UME surface is held at or above +0.2 V (see **Fig. 7**), the AgNP diffuses to the surface, is oxidized, and an electron transfer occurs. An amperometric curve measures amount of current exchanged as a function of time.

The magnitude of current transients depends on the number of electrons transferred in the redox event. Integration of amperometric curves results in summing the charge involved in each redox event, which can be related to number of atoms involved:

$$Q = \int I dt \quad (5)$$

$$N = \frac{Q}{e} \quad (6)$$

where Q is charge, I is current, and e is the elementary charge constant (1.602×10^{-19} C).³⁰

The number of atoms N can be calculated to find the radius r_M of the colliding AgNP:

$$r_M = \sqrt[3]{\frac{3A_r N_M}{4\pi N_A \rho}} \quad (7)$$

where A_r is the relative mass of Ag (107.87 g/mol), N_A is Avogadro's number, N_M is the number of atoms calculated from equation (5), and ρ is the density of Ag (10.49 g/cm³).³⁰

While PIV is useful in providing information about single particles, it ultimately cannot tell us information about the bulk properties of AgNPs in solution. PIV also is

sensitive to particular pH windows and other electrolytes in solution, of which optimization is discussed in the methods section of this thesis.

1.5 UV-Vis Spectroscopy

UV-Vis spectroscopy is a useful characterization tool for AgNPs because a phenomenon known as localized surface plasmon resonance (LSPR) is observed for AgNPs.^{31,32} LSPR is akin to absorbance as they are both detected by an absence of transmitted light, but LSPR occurs due to the oscillation of electrons on the conduction layer of an irradiated substance. Since nanoparticle diameters are smaller than the light wavelengths in the UV-visible region, the particle oscillates with the light and becomes resonant. Once resonant, the particle can absorb energy in the UV and visible region of



Figure 2. AgNP solutions increasing in size from 10 nm to 200 nm (left to right). Image from NanoComposix.³¹

the spectrum. Similar to other metallic ENMs, changes in the size of AgNPs result in changes in the wavelengths of light that enable LSPR and ultimately, a change in color of the solution. As an example, spherical AgNPs have a bright yellow hue in the 5 – 20 nm diameter range, pale yellow at ~40 nm, and silvery pink at 80 nm (**Figure 2.** AgNP solutions increasing in size from 10 nm to 200 nm (left to right). Image from NanoComposix.³¹),³³

Peak absorbance from UV-Vis can be attributed to the wavelength at which AgNPs exhibit optical diffraction.³⁴ Over time, the peak height decreases, correlating to a

decrease of monomeric species in solution. Of the factors affecting the rate of decreasing monomers, the formation of polymeric AgNPs through aggregation is the most prominent. A secondary peak can sometimes be detected at longer wavelengths, which represents the larger, aggregated AgNPs. However, since the aggregated sample has greater heterogeneity in size than the initial monomeric population, the statistical distribution of absorbance peaks is large and often it is difficult to detect an absorbance peak for the aggregated particle. Thus, it is most useful to monitor the peak for the monomeric AgNPs.

From the kinetics data of monomeric particle concentration, the aggregation rate constant k_{agg} can be derived. An equation relating instantaneous rate ($\frac{dA_{\lambda_{max}}}{dt}$) and rate constants (k) was derived by Baalousha et al.:

$$k = \frac{1}{oN} \frac{dA_{\lambda_{max}}}{dt} \quad (8)$$

where o is the optical factor (~ 0.5309), N is the initial concentration of particles, λ_{max} is the peak absorbance wavelength, and t is time.³⁵

1.6 Research Aims

The primary goal of this thesis is to develop a robust and inexpensive analytical method that can detect aggregation of AgNPs *in situ*. Many of the aforementioned techniques either require extensive sample preparation or provide qualitative information about the nanoparticle suspension. As mentioned before, many of the unique transformations with AgNPs that are of interest occur in biological environments. The technique discussed here utilizes two established characterization methods, particle impact voltammetry (PIV) and UV-Vis spectroscopy to obtain nanoscale and bulk scale information simultaneously, not seen in other techniques to date.

Chapter 2: Materials and Methods

2.1 Chemicals

Citrate-capped AgNPs of sizes 10, 20, 40, and 80 nm were sourced from NanoComposix (La Jolla, CA), of both the NanoXact™ (0.02 mg/mL Ag) and BioPure™ (1 mg/mL Ag) product lines. Both products contained AgNPs suspended in a 2 mM sodium citrate solution.^{33,36} See Appendix for lot numbers.

Buffer solutions were prepared using Millipore water (18.2 mΩ) and various salts from Sigma Aldrich: potassium nitrate (≥99.0%), sodium nitrate (≥99.0%), potassium chloride (≥99.0%), sodium chloride (≥99.5% (AT)), and sodium citrate monobasic (anhydrous, ≥99.5% (T)).

Buffers containing 10 mM sodium citrate and 10-100 mM sodium chloride were made each week in Millipore water. Each buffer was pH adjusted up to 5.0 by using 1M NaOH.

2.2 AgNP Size Characterization by DLS and SEM

In-house DLS measurements were completed using a Malvern Zetasizer NanoSeries instrument in NaCl/citrate buffers filtered with 0.20 μm nylon syringe filters. AgNPs were added to buffer and left to sit in the dark for 20 minutes to allow time for the AgNPs to aggregate before measuring the size distribution. The samples were then equilibrated at 25°C for 120 seconds inside the instrument. A backscatter angle of 173° was used. The number of runs collected per experimental replicate was determined automatically and a total of 5 replicates were collected for averaging.

SEM images were obtained using a JEOL 7500F High Resolution SEM at the Nanoscale Characterization Facility in the Singh Center for Nanotechnology at the

University of Pennsylvania. Sizes were processed with ImageJ (National Institutes of Health).

2.3 UV-Vis Parameters

A Cary 100 UV-Vis (Agilent Technologies) spectrophotometer was used for initial UV-Vis characterization. Cary WinUV software was used for instrument control and data collection. Baseline corrections were obtained for both kinetics and spectra. Thirty minutes of lamp warmup was allotted, and the lamp source changeover occurred at 350 nm. A single wavelength was monitored for each size of AgNP (10 nm AgNPs: 390 nm, 20 nm AgNPs: 400 nm, 40 nm AgNPs: 410 nm or 420 nm, 80 nm AgNPs: 455 nm).

For use in the coupled PIV technique, an Ocean Optics Flame UV-Vis spectrophotometer (Ocean Optics) was used with OceanView (version 1.5.7) software for instrument control and data collection. Fifteen minutes was allotted for lamp warmup, followed by baseline corrections. The absorbance spectra were collected using a 6 ms integration time, 10 scans to average, and a boxcar width of 2. Kinetics data was recorded simultaneously by utilizing the spectrophotometer's "strip chart" application. The λ_{\max} was determined through real-time observation of the absorbance spectrum and monitored over time. The strip chart application had a linear buffer of 6000 and was set to update after every 10 scans. Collection through the application began before AgNPs/NaCl was injected such that the decline in λ_{\max} could be observed.

2.4 Electrochemistry Parameters

The electrochemical experiments were run with a three-electrode cell setup: an 11 μm carbon fiber UME working electrode, a platinum wire auxiliary electrode, and an AgCl/Cl reference electrode were used. The working electrode was polished daily with

0.05 μm alumina powder and weekly with 1, 0.3, and 0.05 μm alumina powders.

Between polishing steps, the UME was sonicated in a water bath for 5 minutes. As part of the daily polishing routine, the electrodes were conditioned in citrate buffer by running 200 cyclic voltammetry (CV) cycles from -0.6 V to +0.6 V at a speed of 0.3 V/s.

Before PIV collection, CV sweeps were done for each sample: 2 cycles from -0.6V to +0.6 V with a scan rate of 0.1 V/s. This initial CV sweep is to detect if any residual Ag(I) or AgNPs are present in the cell from previous measurements.

Amperometric curves where voltage is not specified were run at either + 0.3V or + 0.5V and had 5 seconds of quiet time before runs.

For the *in situ* experiments with the 0.02 mg/mL stock AgNPs, buffer was added to the sample cuvette and then AgNPs were pipetted into sample. Before adding AgNPs to the cuvette, the stock solution was briefly vortexed. Immediately after addition, the solution was stirred for approximately 6 seconds and then the amperometric curves were initiated. An alternative procedure was performed in later experiments with the BioPure AgNPs and 5-minute collection times. The AgNPs were first sonicated for approximately 2 minutes, then suspended in 10 mM citrate only buffer. Concentrated salt solution was then injected into the sample, stirred for 6-7 seconds, and then amperometric curves were initiated.

Between experiments, the working electrode was rinsed with deionized water, dried, dipped in 35% nitric acid for approximately 30 seconds, and sonicated in Millipore water for approximately 30 seconds to remove Ag from the surface. The spent electrochemistry cell was replaced with a new cell and all electrodes were rinsed with deionized water and dried with compressed air.

Chapter 3: Characterization of AgNPs

3.1 Characterization by DLS and SEM

To compare sizing data from the UV-Vis/PIV system, auxiliary measurements of the AgNPs were performed using DLS and SEM. DLS was obtained through in-house measurements, while SEM images were obtained at the University of Pennsylvania.

SEM data for all lots were obtained and analyzed using ImageJ. The images in appendix show particles both as distinct spheres and as agglomerated groups (**Figure A1**). Agglomeration of the AgNPs in the SEM sample can be attributed to solution drying: as the citrate buffer dried, the particles were brought into close proximity of each other resulting in apparent agglomeration. DLS measurements obtained for all AgNP lots purchased after acquisition of the DLS instrument. The Stokes-Einstein equation can be applied to DLS light intensity data in order to obtain diffusion coefficients and thus hydrodynamic diameter:

$$D = \frac{k_B T}{6\pi\mu r_H} \quad (7)$$

where D is the diffusion coefficient, k_B is the Boltzmann constant, T is temperature, μ is electrophoretic mobility (a function of zeta potential), and r_H is the hydrodynamic radius of the particle.¹⁰

In all cases, the experimental SEM AgNP diameters agreed with values given by the manufacturer (**Table 1**). With respect to DLS data, all except for lot # CWW0020 agreed with manufacturer values (**Table 2**). CWW0020 has what is likely an aggregate as the primary particle in solution, as well as the most positive zeta potential and a relatively high polydispersity index (PDI). The positivity of the zeta potential indicates the AgNP suspension is relatively unstable, while the PDI indicates that the suspension is more

heterogeneous since it is closer to 1. This result is likely because DLS was run near the end of this lot's lifetime and that the particles sampled were at the bottom of the container, increasing the likelihood of aggregates present in the solution.

Table 1. Experimental AgNP diameters as obtained through SEM images compared to manufacturer values obtained through TEM.

| Lot Number | Manufacturer d_{AgNP} (nm) | SEM d_{AgNP} (nm) |
|------------|-------------------------------------|----------------------------|
| KDP0007 | 9.5 ± 1.8 | 12.7 ± 2.6 |
| SDM0049 | 19.1 ± 3.6 | 21.0 ± 4.3 |
| RRR0001 | 41 ± 5 | 38.3 ± 4.1 |
| PTM0024 | 78 ± 9 | 79.0 ± 6.3 |

Table 2. Average AgNP diameters and zeta potential measurements as obtained through DLS compared to manufacturer values obtained through TEM. *CWW0020 size data taken before zeta potential data*

| Lot Number | Manufacturer d_{AgNP} (nm) | Zeta Potential (mV) | d_{AgNP} (nm) | PdI |
|------------|-------------------------------------|---------------------|------------------------|---------------------|
| CWW0020 | 39 ± 5 | -29.4 ± 1.0 | $60.9 \pm 4.7^*$ | $0.326 \pm 0.012^*$ |
| | | | 103.6 ± 19.3 | 0.403 ± 0.013 |
| PSK0012 | 39 ± 3 | -40.3 ± 1.3 | 43.0 ± 0.5 | 0.120 ± 0.007 |
| PSK0021 | 39 ± 5 | -38.5 ± 0.6 | 48.3 ± 3.6 | 0.174 ± 0.035 |
| PTM0024 | 78 ± 9 | -43.7 ± 0.5 | 87.2 ± 0.7 | 0.091 ± 0.008 |

3.2 Characterization by UV-Vis Spectroscopy

As expected, the AgNPs have near-UV absorbance peaks that are dependent on particle diameter. Large single peaks in the spectra are attributed to the presence of monomeric particles exhibiting LSPR, and the location (wavelength) and broadness of those peaks increases with AgNP size. The 10 nm and 20 nm AgNPs exhibit sharp peaks at approximately 397 and 400 nm respectively. 40 nm AgNPs have peak absorbances at 410 nm or 420 nm depending on lot, while 80 nm AgNPs are the furthest red-shifted, with a peak absorbance at 455 nm (**Figure 3, A**).

Upon AgNP aggregation, the absorbance intensity at the λ_{\max} declines due to a decrease in monomeric particles in solution (**Figure 3, B**). Based on Graham's law of diffusion, 80 nm AgNPs travel the most slowly in solution due to their mass. Once brought in proximity of each other, the 80 nm particles overcome electrostatic repulsions that prevent aggregation more easily than smaller particles due to increased contact time. This results in a faster rate of aggregation with increasing particle size. Since the λ_{\max} can be attributed to the presence of monomeric particles, observation of the λ_{\max} over time provides information about the stability of AgNP monomers, and thus the propensity of AgNPs to polymerize and aggregate.

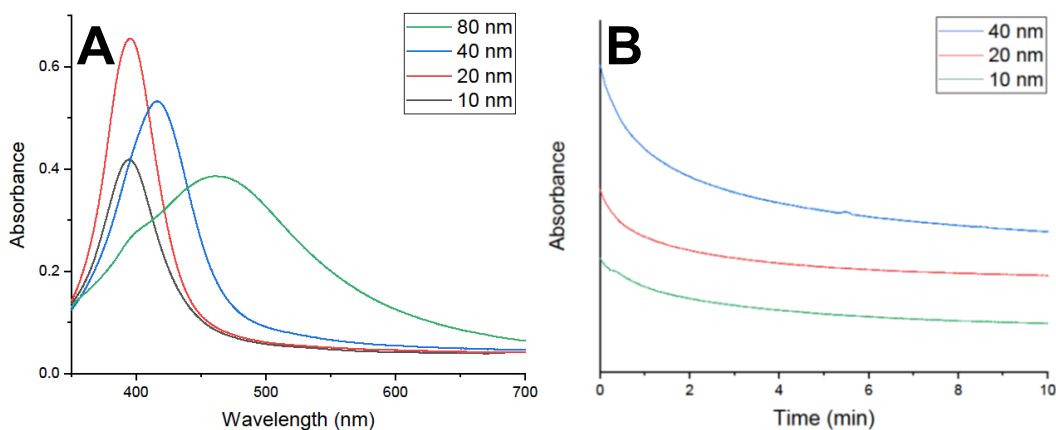


Figure 3. (A) UV-Vis spectra for 10, 20, 40, and 80 nm AgNPs and (B) Offset kinetics data for 10, 20, and 40 nm AgNPs.

Kinetics data was variable—often times there were issues with AgNPs mixing into solution, shown by the fluctuation in λ_{\max} (**Figure 4, A**) However, suspending AgNPs in citrate buffer before the addition of NaCl seemed to solve the issue of reproducibility in kinetic data (**Figure 4, B**). Optimization of signal averaging also contributed to clean spectra and kinetics.

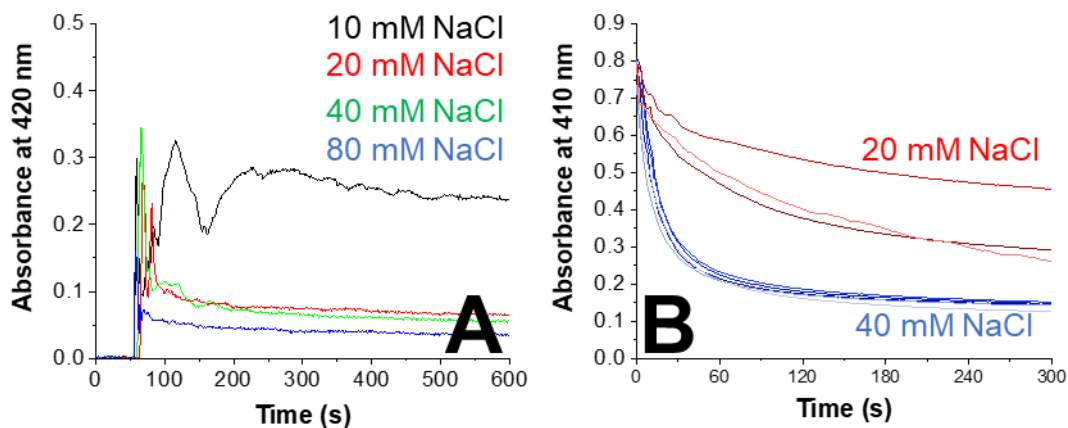


Figure 4. Representative kinetics curves at various concentrations of NaCl (A) before and (B) after optimization attempts. A is offset for clarity.

3.3 Electrochemical characterization

Optimization of PIV as a standalone technique was performed to obtain reproducible amperometric curves. This involved optimization of solution conditions, exploration of various AgNP sizes, and determination of the reduction potential for AgNPs.

Key components of reducing noise were procedural as well as intrinsic to the

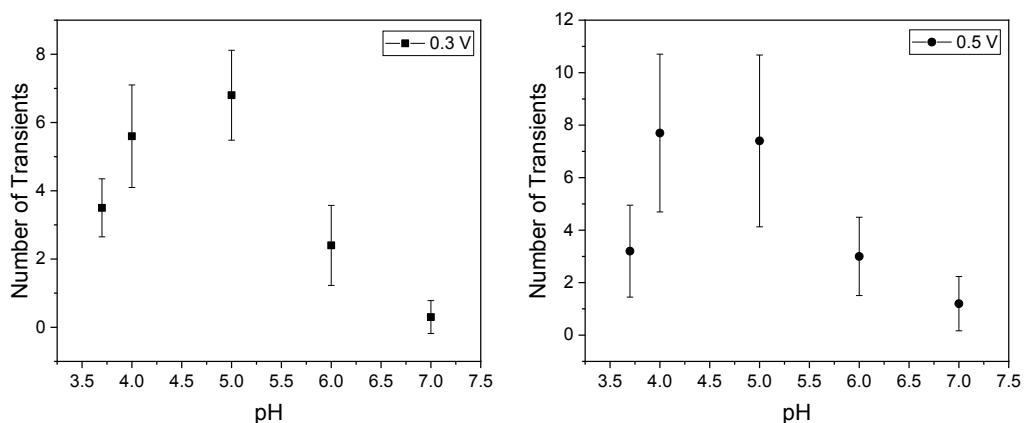


Figure 5. Number of transients observed as a function of pH, showing a clear tapering effect at the ends of the pH range (3.7 to 7.0). Averages from several 1-minute scans of 40 nm AgNPs suspended in 10 mM NaCl 10 mM citrate buffer at potentials of (A) +0.3 V and (B) +0.5 V.

composition of the cell solution. The presence of oxygen must be minimized as it increases the background current (lowers the signal-to-noise) and interferes with the current transients obtained from the direct oxidation of AgNPs. As a result, airtight caps were used, and the solution was purged and blanketed with a continuous stream of nitrogen gas. Salt concentration and composition also contributed to system noise. Lack of sufficient electrolytes in the solution contributes to a background current, increasing noise and false transients in PIV systems.³⁷ NaCl consistently exhibited the least noise compared to the other salts tested (MgCl₂, KCl, NaNO₃, and KNO₃). A lower limit of 10 mM NaCl was optimal to reduce background current. Additionally, the pH of the solution affects detection of transients. pH optimization was performed in 10 mM NaCl over the range 3.7 – 7.0 pH units (**Figure 5**). The largest number of transients was observed with a 10 mM sodium citrate, 10 mM NaCl solution at pH 5.0.

Once solution conditions were optimized, a range of AgNP sizes was tested. Decreasing particle size increased the number of transients present in a scan due to differences in the concentrations of the particles and in their rates of diffusion. For example, more transients are observed for 40 nm AgNPs compared to 80 nm AgNPs over a 1 minute time frame (Figure 5, blue and green traces, respectively). The reported concentrations of particles are with respect to total Ag in solution instead of the particle concentration. For example, the NanoXact particles contain 0.020 mg/mL of Ag (**Table A1**) regardless of nanoparticle size. The molar particle concentrations are 6.0×10^{-9} M 10 nm AgNPs, 7.6×10^{-10} M 20 nm AgNPs, 9.4×10^{-11} M 40 nm AgNPs, and 1.2×10^{-11} M 80 nm AgNPs. The diffusion coefficients of the AgNPs also affect the number of

transients observed. The larger the AgNP, the smaller the coefficient of diffusion, and the less frequently the transients are observed.

AgNP size directly affects the transient height. The larger the particle, the greater the number of silver atoms that are oxidized at the electrode upon impact, and the greater the magnitude of the current transient (**Figure 6**). A high signal-to-noise ratio is observed

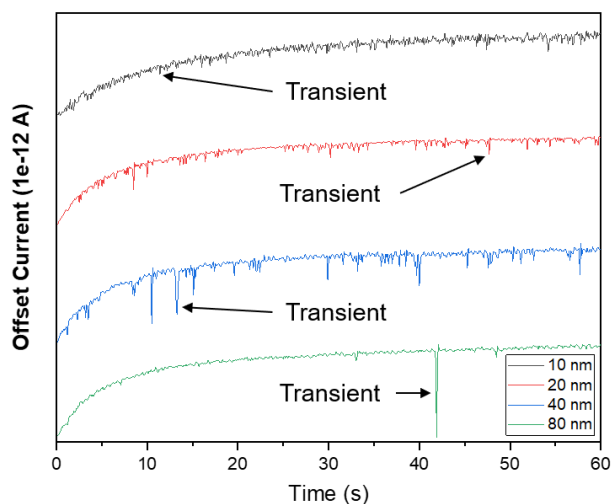


Figure 6. Sample amperometric curves for 10, 20, 40, and 80 nm AgNPs. Signal-to-noise increases with particle diameter while transient frequency decreases. Curves are offset for clarity and sample transients are highlighted.

with large particles, which enables better integration of transient peaks and determination of a size distribution. Although larger particles have higher signal-to-noise ratios, the frequency of impacts is very low. High

transient frequency is desirable because it allows for better statistical determination of size

distributions. Low transient frequency can also bias aggregation data over time—since small particles have shorter diffusion times to the electrode than the aggregates forming in solution, more small transients than large transients are detected at later time points. The 40 nm AgNPs were found to be the best compromise between signal-to-noise ratio and transient frequency, and were chosen for further aggregation studies.

While the current transients have so far been ascribed to direct oxidation of an AgNP, it is crucial to be able to differentiate between faradaic and non-faradaic current

events that may occur in solution. Non-faradic events are primarily comprised of background current from other electrolytes, such as salt ions in the buffer.³⁷ Measuring transient peak height as a function of potential can be used to distinguish faradaic events from noise.³⁸

At potentials more negative than the reduction potential of silver (+ 0.2 V vs. Ag/AgCl), few to no transients were observed for the 20 nm, 40 nm, and 80 nm AgNPs (**Figure 7**). As the potential was increased in the positive direction, the number of current transients increased drastically. The 20 nm and 40 nm AgNPs have a clear “turn on” potential at + 0.15 V and 80 nm AgNPs at + 0.20 V (**Figure 7**). No “turn on” potential was observed for the 10 nm AgNPs; as previously shown in **Figure 6**, the low signal-to-noise prevents analysis by this method, consistent with findings stating that 10 nm AgNPs are in the lower limit of reliable sizing using PIV.³⁹ Overall, this experiment provided information on the best potential to observe AgNP current transients, of which + 0.5 V and + 0.3 V were chosen. Initially, + 0.5 V was chosen for most experiments because the higher potential was well beyond the turn-on point. However, this sufficiently high oxidizing potential can erode the UME surface with long-term use, so a less oxidizing potential, + 0.3 V, was selected going forward.⁴⁰

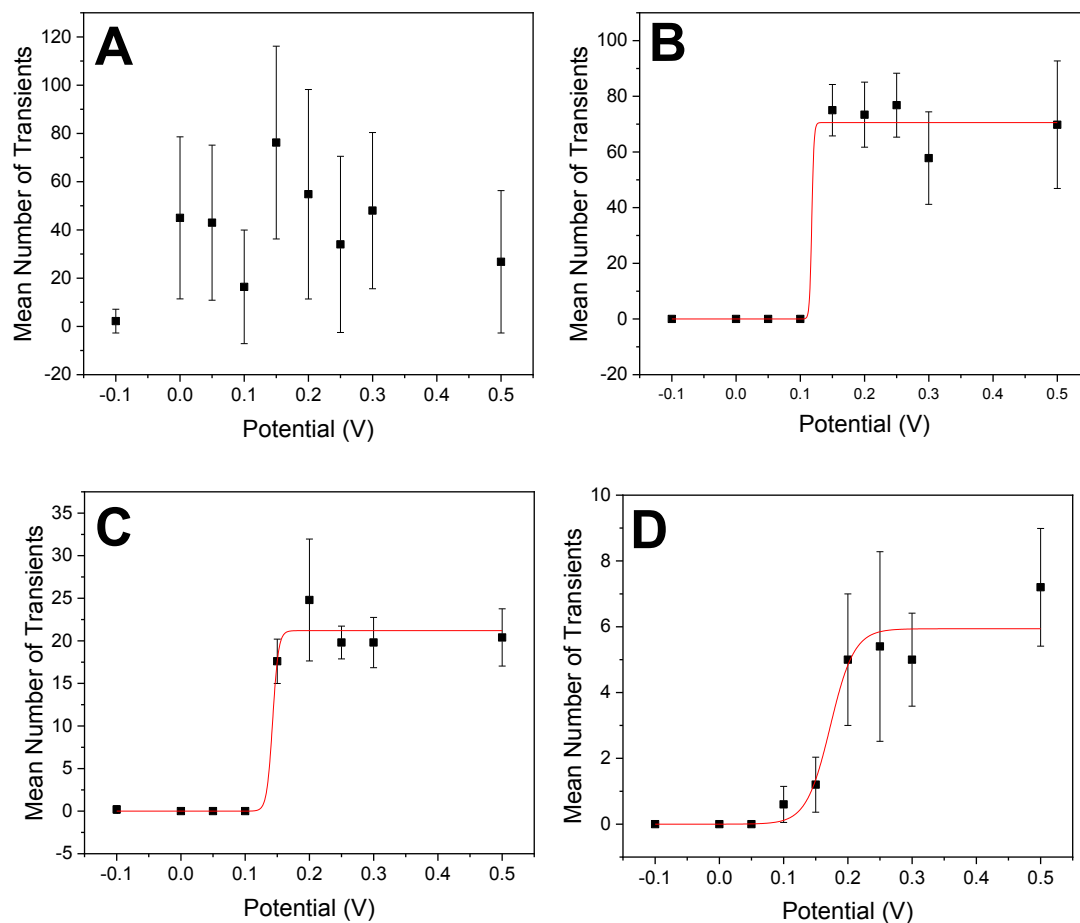


Figure 7. Faradaic Curves obtained for (A) 10 nm, (B) 20 nm, (C) 40 nm, and (D) 80 nm AgNPs. At ~ 0.15 V, the 20 nm and 40 nm AgNPs show transients, indicating that potential as a “turn-on” point for the oxidation of the particles. The point for 80 nm AgNPs appears to be shifted to ~ 0.20 V. No sigmoidal relationship was obtained for the 10 nm particles.

Chapter 4: Merging Techniques

The ultimate purpose of this thesis is to combine two experiments that describe AgNP aggregation—PIV and UV-Vis spectroscopy—into one integrated method. Through concurrent collection, a more comprehensive aggregation model can be obtained than by using the methods independently.

4.1 Development of hybrid cell

The traditional cylindrical electrochemical cell used for PIV was not compatible with the UV-Vis cuvette holder, so a hybrid sample cell had to be developed. The most facile way to accomplish this was to retro-fit a standard UV-Vis cuvette for use with PIV. This cell required a custom cap to be designed such that the electrodes could be immersed in solution without blocking the light path of the spectrophotometer.

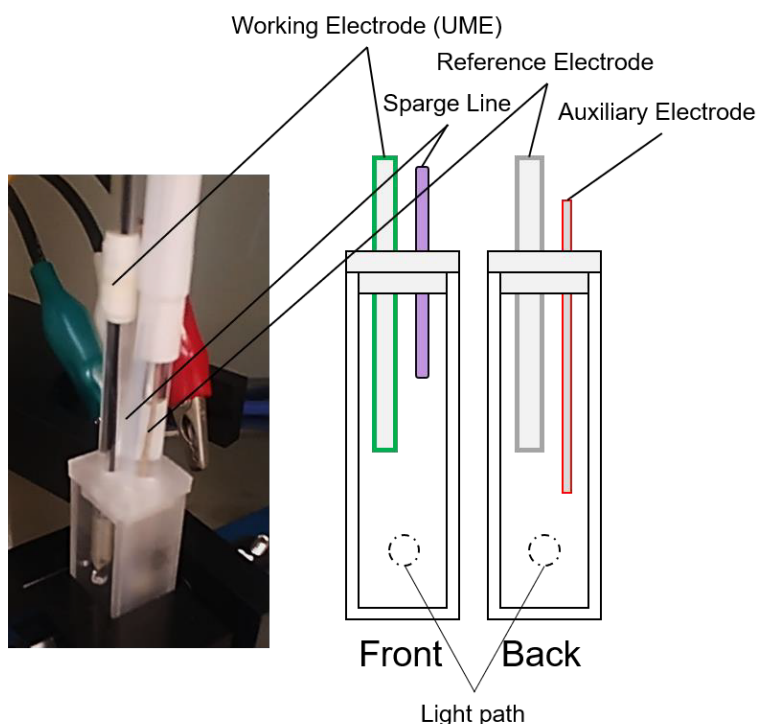


Figure 8. Image and diagram depicting spectroelectrochemical cell and its components. Electrodes and sparge tube rest above light path of spectrophotometer.

Spectroelectrochemical cells designed for simultaneous electrochemical and spectroscopy experiments exist, but these cells are designed with specialized, mesh working electrodes.⁴¹ Mesh electrodes allow for the spectrophotometer's light path to be unimpeded, but

the surface area of such an electrode is very large with respect to an AgNP and cannot be used for PIV. Thus, a hybrid cell that utilized the same three-electrode setup for PIV, including an UME as the working electrode, but with the electrodes arranged in a UV-Vis cuvette had to be constructed (**Figure 8**).

There were two proposed methods for fabricating the cuvette cap to hold the electrodes; either the cap would be made by drilling holes into a pre-existing cuvette cap, or the cap would be printed using 3D printing technologies. For the sake of higher precision and greater ease of production, the latter was chosen. Printing the cap was efficient—within three hours, nine caps were printed, more than what would be needed for day-to-day data collection. Polycarbonate was selected as the cap material because of its resistance to contact

with dilute nitric acid, a solution used in cleaning all electrochemistry glassware.⁴² It has been noted that extended, continuous exposure to

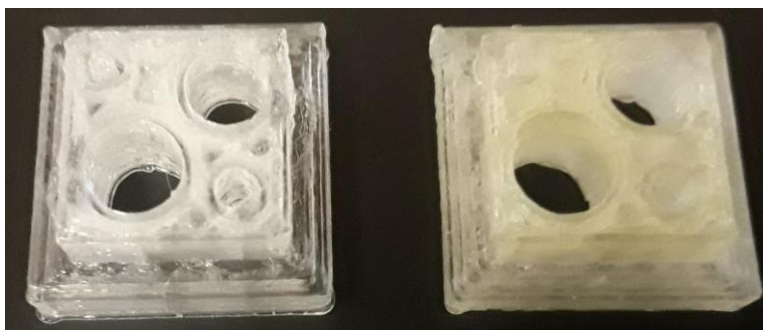


Figure 9. Printed-polycarbonate caps before and after extended submersion in dilute (~5%) nitric acid.

nitric acid results in yellowing of the caps (**Figure 9**), but so far this has not adversely affected the performance of the cell. Consequently, the cleaning procedure for the caps was altered such that they would be submerged in nitric acid for a maximum of 24 hours.

From an initial design attempt (**Figure 10**, Model 1) it was found that the largest hole (meant to house the reference electrode) was too near the edges of the cap and could not be printed accurately due to resolution restrictions. The hole placement also brought

the electrodes in such close proximity that they were in physical contact and interfered with data collection, so a second model was constructed (**Figure 10**, Model 2). The hole for the reference electrode was moved inward and hole diameters and base units (mm) were corrected such that the electrodes and sparge tube would have an improved fit. Although the spacing of the electrodes was improved from the previous design, the electrodes would not fit through the holes in the cap. In the process of printing the caps, the PC shrank as it cooled, resulting in the holes being slightly cone-shaped. Because the holes were measured to have a snug, airtight fit, the shrinking phenomenon proved to be an issue. Additional drilling of the holes was done such that they were cylindrical. The final sample cell used for simultaneous PIV and UV-Vis experiments is depicted in

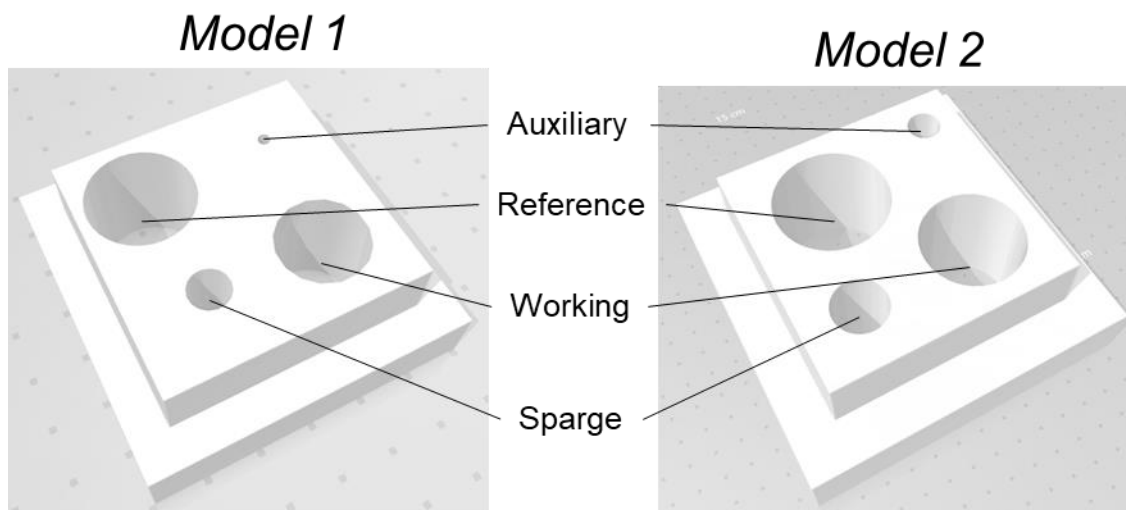


Figure 10. 3D digital models for the spectroelectrochemical cap. Both modeled with Rhino 3D then printed in polycarbonate (PC) material with an Ultimaker 3 printer.

Figure 10, Model 2.

4.2 Proof-of-Principle Aggregation Experiments

Once the spectroelectrochemical cap was constructed, both UV-Vis and PIV techniques were performed in the cell to assure the reliability of the techniques with the new configuration. Absorbance data was collected and compared with previously-obtained spectra, with no noticeable change in SPR peak quality or location (**Figure 11**).

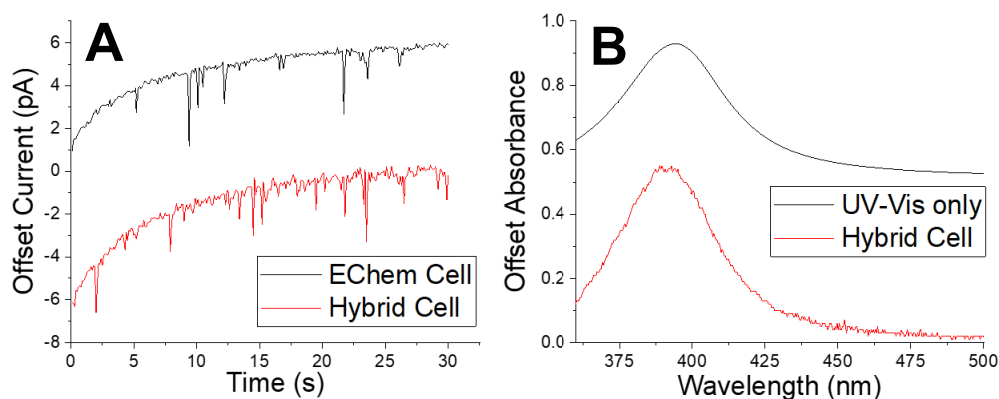


Figure 11. (A) Absorbance scans of AgNPs in UV-Vis only spectrometer and hybrid cell setup. (B) Amperometric curves of PIV only cell and hybrid cell setup.

PIV curves were compared as well, again with no noticeable changes in quality of the amperometric curves (**Figure 11**).

Next, both techniques were performed simultaneously, which was especially necessary as the potential for these collection methods to affect each other is non-negligible. The following data sets were obtained concurrently: PIV curves, UV-Vis spectra, and UV-Vis kinetics curves. Initially, the collection of PIV data was done in relatively short, 30 second periods while kinetic collection lasted for approximately two hours. The kinetics curve was unaffected, as there were no discontinuities in curve quality when PIV was running versus when it was not. Conversely, while UV-Vis collection was occurring, continuous PIV collection was not affected. Finally, amperometric curves were compared with and without the UV-Vis lamp turned on and there was no clear difference between the curves. These experiments demonstrated that

neither technique affected the data quality of the other, even when run in concert. A representative sample output from simultaneous PIV and UV-Vis collection is shown in **Figure 12**.

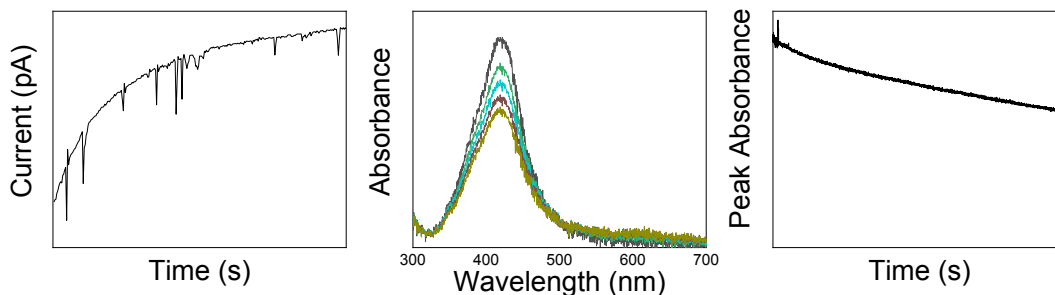


Figure 12. Sample collection of PIV, UV-Vis spectra, and kinetics.

4.3 Optimizing the Performance of the Integrated PIV and UV-Vis Technology for Monitoring AgNP Aggregation

A model aggregation study was completed to test the utility of the coupled PIV and UV-Vis technique. The data can be split into two collection time-frames; one spread over a long time period (30 minutes up to 2 hours), and one over a short time period (5 to 10 minutes). The long-term aggregation study was first undertaken in hopes of replicating findings found in literature using this method.⁴³ However, this study was not consistently reproducible, with particularly variable kinetic data. Still, some qualitative conclusions can be made from these data. As observed in **Figure 13 A**, the average diameter of AgNPs (as determined via PIV) seems to decrease slightly then increase over 10 minutes. After 10 minutes, few if any transients are detected, suggesting that the majority of particles have a longer diffusion time to the electrode than the 1-minute long intervals used for data collection or have crashed out of solution. The UV-Vis data does show that the absorbance associated with the AgNP monomer generally declines, though an unexpected slight increase in absorbance (beyond 600 seconds) is observed for the

second data set. A smooth, continuous curve is expected to be observed with kinetics data, but this is not observed, instead there is semi-rapid fluctuation in the curve that made it difficult to fit. The curves in **Figure 13 C** are in fact the smoothest representatives for these 30-minute studies; examples not shown here exhibited more significant and random fluctuation patterns.

Because of the unreliable sizing data obtained through the previous experimental setup, the procedure was changed so that PIV and UV-Vis were both run continuously. Previously, 10 replicates of 30-second PIV scans occurred at set time points, with wait periods between points (*e.g.*, 10 replicates after injection, wait 10 minutes, 10 replicates again). A possible benefit of collecting PIV continuously was that aggregates with longer migration times could now be detected. Additionally, since the kinetics data fitting

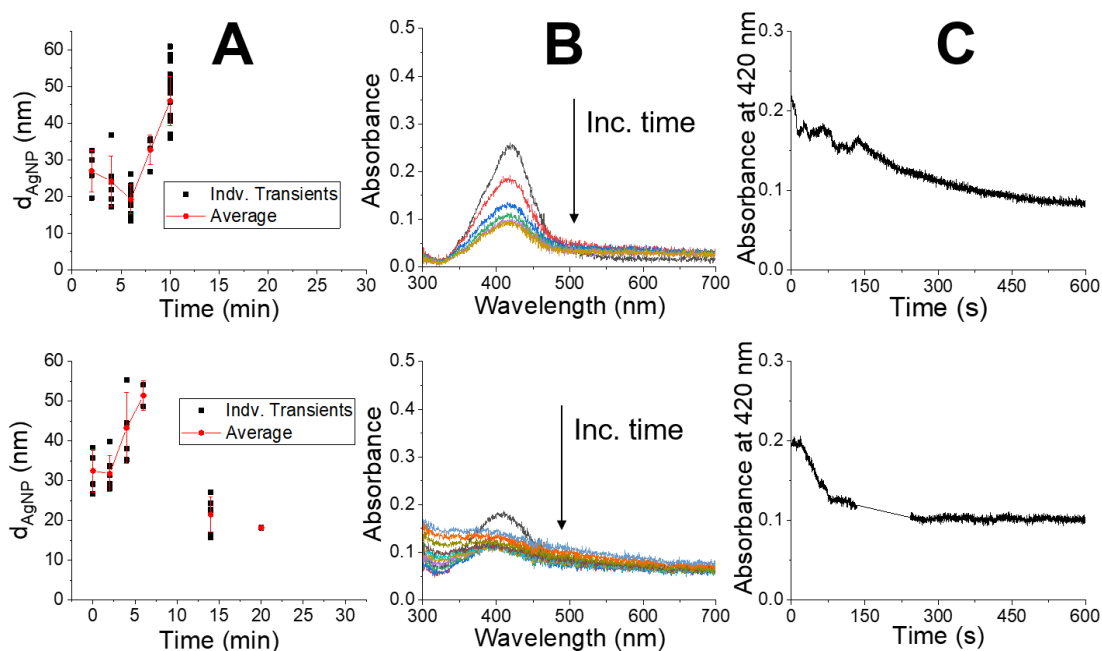


Figure 13. Data collected from two 30 minute aggregation studies with 40 nm particles in 40 mM NaCl 10 mM citrate solution: (A) size of AgNPs as determined by PIV, (B) UV-Vis spectra collected every 2 minutes (time <10 min) and every 5 minutes (time >10 min), and (C) kinetics data at the lambda max, about 420 nm. Arrow indicates increasing time.

assumes that early aggregation is mostly due to dimerization (Section 1.2), the collection time was shortened to the first 5-10 minutes.

The short-term experiments were more reproducible, with the best results occurring with 5-minute continuous PIV and accompanying UV-Vis collection. With respect to PIV in this system, 20 mM NaCl solution indicates not much change in average particle diameter (**Figure 14 A**), corresponding with the moderate change in the absorbance spectra (**Figure 14 B**). PIV of the 40 mM NaCl solution showed relatively constant average particle diameter (**Figure 14 C**), but a significant and rapid decrease in the absorbance spectra (**Figure 14 D**). A closer inspection of the PIV data shows that the amount of monomeric AgNPs in the 40 mM NaCl solution has decreased.

Kinetic data for 40 nm AgNPs in various salts was obtained. Qualitatively, the absorbance declines sharply with time after the CCC has been reached (>20 mM NaCl).

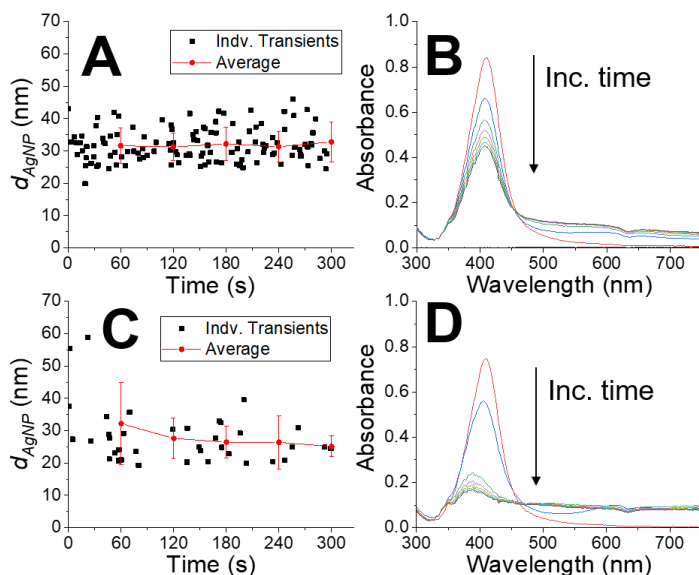


Figure 14. Representative data of 40 nm particles in (A-B) 20 mM and (C-D) 40 mM NaCl solution. PIV transient points are spread continuously over the entire collection period, with average d_{AgNP} at 60-second intervals. Spectra taken every 60 seconds.

The corresponding spectra corroborate this: the λ_{max} does not shift horizontally until absorbance reaches 0.2 (**Figure 14 B, D**), only the absorbance is lessened with time.

It is also important to note that occasionally a second peak is observed in the UV-Vis spectra,

attributed to aggregates exhibiting SPR. Simultaneous collection of the aggregate peak and the monomer peak is possible with the UV-Vis spectrophotometer, however, since the aggregate peak is not consistently observed across replicates, only the monomer peak was monitored.

Several optimization experiments were done to obtain smooth UV-Vis kinetics curves that could be fitted to obtain rate constants. An approach to fitting the kinetics data was through measuring the initial slope, which for this experiment was found to be the most linear in the first 15 seconds (**Figure 15, A**). Equation 8 (Section 1.5, reproduced below) was used to extract a k_{agg} from the slope:

$$k = \frac{1}{oN} \frac{dA_{\lambda_{max}}}{dt} \quad (8)$$

Overall, the k_{agg} values increase with NaCl concentration, as expected (**Table 3**). From 20 mM to 40 mM NaCl, the k_{agg} value almost triples, but from 40 mM to 80 mM

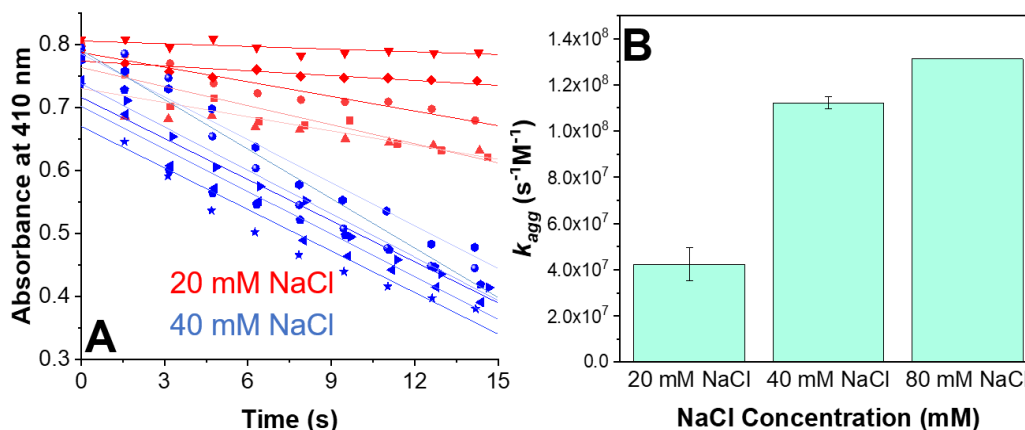


Figure 15. (A) Initial UV-Vis kinetics data and (B) kinetics constants obtained for 40 nm AgNP aggregation experiments in 20 and 40 mM NaCl, 10 mM citrate buffer. $\lambda_{max} = 410$ nm. *80 mM NaCl does not yet have replicates. *

k_{agg} increases by 2×10^7 s⁻¹M⁻¹. This may be solved by data averaging as the 80 mM NaCl does not have sufficient replicates at the time of writing.

Table 3. Linear fit parameters for 40 nm AgNP kinetic data in various NaCl concentrations.

| [NaCl] (mM) | y-intercept | dA/dt (s ⁻¹ ×10 ⁻²) | <i>k_{agg}</i> (s ⁻¹ M ⁻¹ ×10 ⁷) | Average R ² |
|----------------|---------------|--|---|------------------------|
| 20 | 0.760 ± 0.029 | 0.845 ± 0.34 | 4.23 ± 0.72 | 0.84337 |
| 40 | 0.722 ± 0.042 | 2.24 ± 0.05 | 11.2 ± 0.3 | 0.95005 |
| 80 | 0.791 | 2.62 | 13.1 | 0.94727 |

DLS measurements were obtained and averaged for 40 nm AgNPs in various salt solutions to compare with the PIV and UV-Vis analysis (**Table 4**). The 10 mM NaCl had the smallest d_{AgNP} and most positive zeta potential, as expected. 20 mM NaCl also had little effect on the d_{AgNP} , as the sizes are comparable to 10 mM. Interestingly, the 40 mM and 80 mM NaCl trials show similar zeta potentials, but starkly different diameters. The similarity in values between 40 mM and 80 mM NaCl is also reflected in the k_{agg} obtained through UV-Vis (**Table 3**). The PDI for 20 mM and 40 mM NaCl are twice as large as the rest of the salt concentrations (0.433 and 0.475, **Table 1Table 4**), indicating the particle suspension is non-homogeneous and multiple aggregate sizes are present.

Table 4. Average particle diameters of 40 nm AgNPs after exposure to salt buffers. The CCC of 40 nm AgNPs was between 20 and 40 mM. Lot #PSK0012.

| [NaCl] (mM) | Zeta potential (mV) | d_{AgNP} (nm) | PDI |
|----------------|------------------------|--------------------|---------------|
| 10 | -40.6 ± 0.6 | 46.3 ± 2.2 | 0.234 ± 0.011 |
| 20 | -43.3 ± 1.4 | 49.7 ± 2.5 | 0.433 ± 0.005 |
| 40 | -48.2 ± 1.9 | 54.1 ± 0.7 | 0.475 ± 0.027 |
| 80 | -49.9 ± 2.3 | 403.1 ± 19.8 | 0.266 ± 0.020 |
| 100 | -53.7 ± 1.5 | 479.6 ± 27.4 | 0.283 ± 0.025 |

When initially comparing UV-Vis and DLS data with data obtained with PIV, there appears to be a lack of agreement; the former two methods indicate significant aggregation of 40 nm AgNPs in NaCl solutions while this PIV data indicates no statistically significant change in particle diameter, and thus no aggregation. One factor to

consider when rationalizing the PIV data is that the method is biased toward smaller particles. A study by Xie et al. has recently shown that the reliable detection limit of AgNP size using PIV is up to 100 nm.⁴⁴ As shown in **Table 4**, the aggregate sizes determined by DLS in 80 mM NaCl are greater than 400 nm, and in previous DLS collection, it has been shown that 40 mM AgNPs have sizes over 170 nm (**Table A4**). Since PIV relies on AgNPs diffusing to the UME, and larger particles have increased diffusion times, more small particles can diffuse to the UME within a set time frame. This would explain why PIV seems to be “missing” aggregate transients and be biased toward transients indicative of monomeric 40 nm AgNPs.

Because of the bias of PIV toward smaller particles, plotting the transient frequency then is a more accurate view of AgNP aggregation. When plotted, there seems to be a relationship between transient frequency and salt concentration similar to the relationship between k_{agg} value and concentration (**Figure 16**). If so, this may indicate that PIV could potentially provide data that is reflective of kinetics, and a new model could be developed.

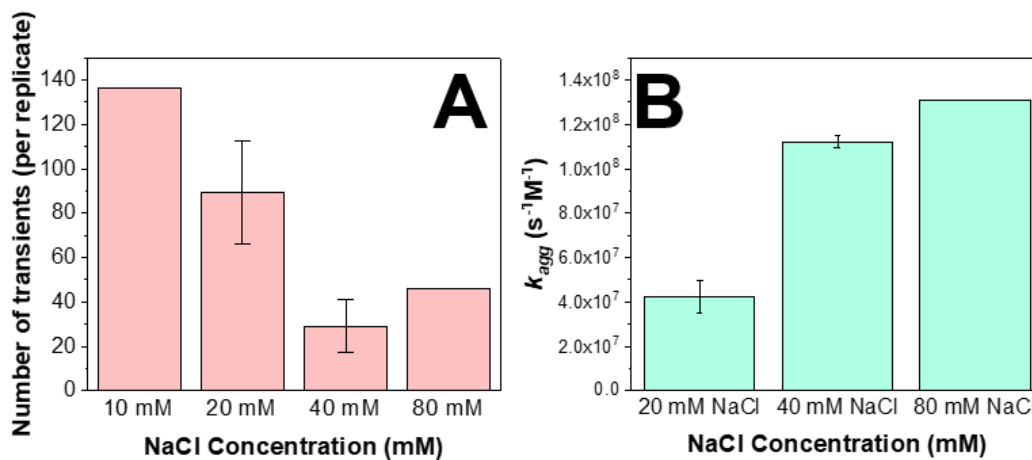


Figure 16. (A) Initial UV-Vis kinetics data and (B) kinetics constants obtained for 40 nm AgNP aggregation experiments in 20 and 40 mM NaCl, 10 mM citrate buffer. $\lambda_{max} = 410$ nm. *80 mM NaCl does not yet have replicates.*

Chapter 5: Conclusions and Future Directions

To better understand transformations of AgNPs, namely aggregation, a method combining the strengths of UV-Vis spectroscopy and PIV was developed. This system provides information about AgNP transformations both on a particle level and on a bulk scale. To do this, a custom cap for simultaneous collection was designed and tested. Neither technique was found to affect the other significantly, and data was successfully collected. Sizing data that agreed with manufacturer values of non-aggregated, 40 nm particles was obtained using this joint method.

A sample study to measure aggregation using the combined method was done by increasing NaCl concentration. Here, the results from the UV-Vis part of the system qualitatively indicate aggregation, while PIV results indicate aggregation semi-quantitatively. The decrease of transients observed seems to be correlated to k_{agg} values, so a model relating kinetics to PIV could potentially be developed. Separate DLS data on the suspensions more quantitatively confirmed aggregation of the AgNPs in solution. A future goal is to optimize PIV collection and conditions such that information about aggregate size can be obtained without being lost to monomeric particle bias.

To develop the system even further, test studies with other standardized ENMs could be done. Varying shape of the ENM may change transient distributions as well as how aggregation or other induced transformations affect the UV-Vis spectra and kinetics. Additionally, using functionalized AgNPs (AgNPs with other capping agents, shelled particles, etc.) would provide more information on the system's robustness.

Beyond studying NaCl solutions as a sample system, this methodology could be applied to studying more complex environments. One such environment is the presence

of natural organic matter (NOM). By measuring how the transient quality and frequency change with and without adsorbed NOM, PIV could provide real-time information that informs the data provided simultaneously by UV-Vis.

Acknowledgements

I would like to thank the Academy—

In actuality, there are many people that helped me through the process of researching and writing this thesis. Firstly, I'd like to thank the Riley Lab: Dr. Kathryn Riley for being an amazing PI, advisor, and mentor; Arka Rao '18 for being a great first lab mate and senior member that I could come to; Zachary O'Dell '20 for being another great lab mate and lab DJ for much of the summer I spent developing this research; Dan Bohelmer '20, Janan Hui '20, and Hee-Yon Park '20 for being awesome lab mates during the academic year.

I would also like to thank the Chemistry Department at Swarthmore for providing me with the opportunity to pursue this research as well as providing me with support and teaching. Thank you to Drs. Kathleen Howard, Kyle Wagner, and Kathryn Riley for serving on my thesis committee and providing me with helpful feedback. Thank you as well to Swarthmore College for providing me with a generous summer research fellowship that made this research possible.

Thanks to Andrew Reuther, Doug Willen, Russell Prigodich, and J. Johnson for assisting me with the process of creating the spectroelectrochemical cap: everything from consultation, taking measurements, 3D printing, and drilling. I'd also like to thank the Swarthmore Makerspace and Engineering Department shop for providing me with the materials and tools to produce the caps.

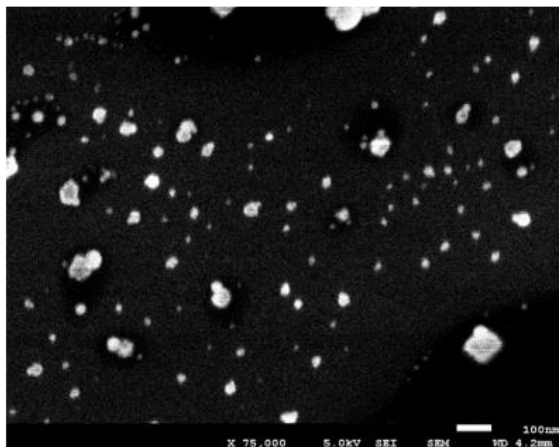
Lastly, I would like to thank my friends and family for supporting me throughout this research and beyond. Fellow chemistry students Abigail Wong-Rolle '19 and Mackinsey Smith '19 were great buds to write theses with, as were the rest of the chemistry department's graduating class. Close friends I've made outside of the department have also helped me keep going in this process, and I thank them for their moral support.

Appendix

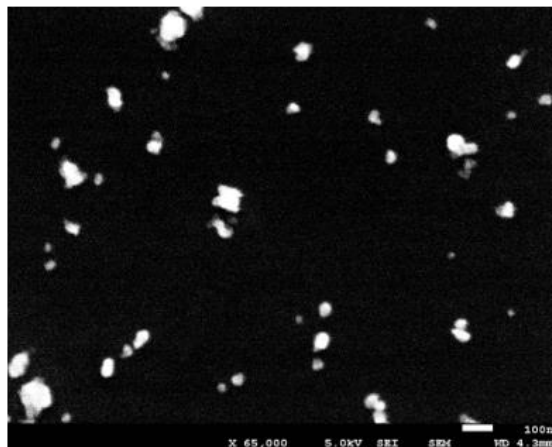
Table A 1. AgNP lots ordered from NanoComposix. All are suspended in 2 mM citrate.

| d_{AgNP} (nm) | Concentration (mg/mL) | Lot Number |
|--------------------|--------------------------|------------|
| 10 | 0.02 | KDP0007 |
| 20 | 0.02 | SDM0049 |
| 40 | 0.02 | RRR0001 |
| 40 | 0.02 | PSK0021 |
| 40 | 1.0 | CWW0020 |
| 40 | 1.0 | PSK0012 |
| 80 | 0.02 | PTM0024 |

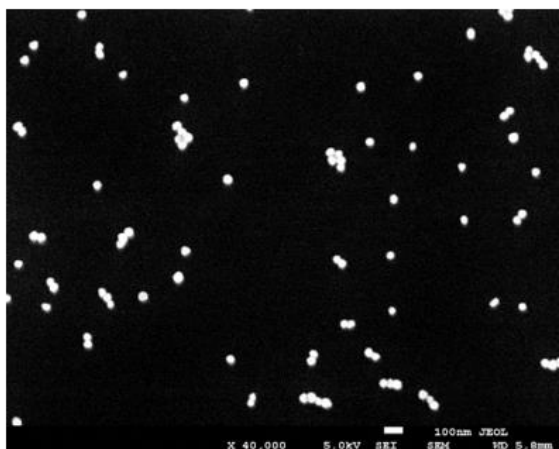
KDP0007 – 10nm



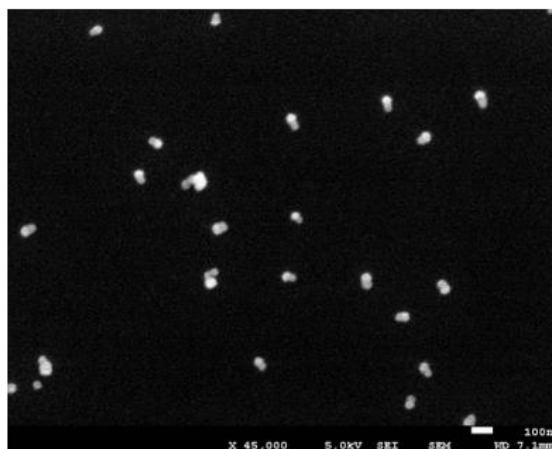
SDM0049 – 20 nm



PSK0021 – 40 nm



RRR0001 – 40 nm



PTM0024 – 80 nm

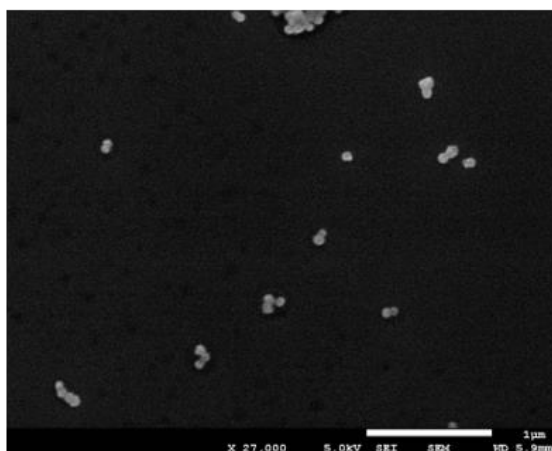


Figure A1. Representative SEM images for AgNP lots.

An exponential decay model fit the 40 nm AgNPs in 20 mM and 40 mM NaCl kinetics data best:

$$y = y_0 + A_1 e^{-x/t} \quad (9)$$

where y_0 is the offset, A_1 is amplitude, and t is time constant.⁴⁵ From this, one can obtain the decay rate of absorbance, $1/t$. If solved with the same treatment as the tangent lines, the “ k_{agg} ” values suggest that aggregation increases with NaCl concentration, as expected (Table A2). However, this fit is not well supported in literature, and thus cannot be used for comparison.

Table A2. Exponential decay fit parameters for 40 nm AgNP kinetic data in various NaCl concentrations. Fits had high average R^2 values.

| [NaCl] (mM) | y_0 | A_1 | t | “ k_{agg} ” ($s^{-1}M^{-1} \times 10^7$) | Average R^2 |
|----------------|-------------------|-------------------|----------------|---|---------------|
| 20 | 0.447 ± 0.011 | 0.277 ± 0.010 | 30.7 ± 3.2 | 17.6 ± 0.6 | 0.9791 |
| 40 | 0.215 ± 0.005 | 0.535 ± 0.006 | 14.7 ± 1.4 | 34.2 ± 0.3 | 0.9955 |
| 80 | 0.269 | 0.553 | 12.7 | 39.3 | 0.9897 |

An allometric fit exactly following the rate law was also attempted:

$$A = A_0 e^{-kt} \quad (10)$$

R^2 values were overall worse than the exponential decay fits, but still above 0.9 (Table A3). Another discrepancy is that allometric k_{agg} values are an order of magnitude higher than the exponential decay k_{agg} values; and 40 mM NaCl has the highest k_{agg} value as opposed to the expected 80 mM NaCl.

Table A3. First-order fit parameters for 40 nm AgNP kinetic data in various NaCl concentrations.

| [NaCl] (mM) | A_0 | k_{agg} (s⁻¹) | Average R² |
|------------------------|-------------------------|--|------------------------------|
| 20 | 0.810±0.013 | 0.120±0.005 | 0.91554 |
| 40 | 0.942±0.030 | 0.337±0.011 | 0.94850 |
| 80 | 1.01±0.02 | 0.323±0.008 | 0.97349 |

Table A4. DLS size data for 40 nm AgNPs in select NaCl concentrations. Lot #PSK0021.

| [NaCl] (mM) | d_{AgNP} (nm) | PdI |
|------------------------|---------------------------------------|---------------|
| 20 | 40.7 ± 0.6 | 0.445 ± 0.006 |
| 40 | 176.3 ± 10.1 | 0.269 ± 0.015 |
| 100 | 229.6 ± 3.7 | 0.291 ± 0.008 |

References

- (1) Calderón-Jiménez, B.; Johnson, M. E.; Montoro Bustos, A. R.; Murphy, K. E.; Winchester, M. R.; Vega Baudrit, J. R. Silver Nanoparticles: Technological Advances, Societal Impacts, and Metrological Challenges. *Frontiers in Chemistry* **2017**, *5*. <https://doi.org/10.3389/fchem.2017.00006>.
- (2) Vance, M. E.; Kuiken, T.; Vejerano, E. P.; McGinnis, S. P.; Hochella, M. F.; Rejeski, D.; Hull, M. S. Nanotechnology in the Real World: Redeveloping the Nanomaterial Consumer Products Inventory. *Beilstein Journal of Nanotechnology* **2015**, *6*, 1769–1780. <https://doi.org/10.3762/bjnano.6.181>.
- (3) Yang, Y.; Westerhoff, P. Presence in, and Release of, Nanomaterials from Consumer Products. In *Nanomaterial: Impacts on Cell Biology and Medicine*; Capco, D. G., Chen, Y., Eds.; Advances in Experimental Medicine and Biology; Springer Netherlands: Dordrecht, 2014; pp 1–17. https://doi.org/10.1007/978-94-017-8739-0_1.
- (4) Market report on emerging nanotechnology now available | NSF - National Science Foundation https://www.nsf.gov/news/news_summ.jsp?cntn_id=130586 (accessed Dec 13, 2018).
- (5) Pourzahedi, L.; Vance, M.; Eckelman, M. J. Life Cycle Assessment and Release Studies for 15 Nanosilver-Enabled Consumer Products: Investigating Hotspots and Patterns of Contribution. *Environ. Sci. Technol.* **2017**, *51* (12), 7148–7158. <https://doi.org/10.1021/acs.est.6b05923>.
- (6) Vasileiadis, S.; Brunetti, G.; Marzouk, E.; Wakelin, S.; Kowalchuk, G. A.; Lombi, E.; Donner, E. Silver Toxicity Thresholds for Multiple Soil Microbial Biomarkers. *Environ. Sci. Technol.* **2018**, *52* (15), 8745–8755. <https://doi.org/10.1021/acs.est.8b00677>.
- (7) Li, X.; Lenhart, J. J. Aggregation and Dissolution of Silver Nanoparticles in Natural Surface Water. *Environ. Sci. Technol.* **2012**, *46* (10), 5378–5386. <https://doi.org/10.1021/es204531y>.
- (8) Liu, H.; Zhong, L.; Yun, K.; Samal, M. Synthesis, Characterization, and Antibacterial Properties of Silver Nanoparticles-Graphene and Graphene Oxide Composites. *Biotechnol Bioproc E* **2016**, *21* (1), 1–18. <https://doi.org/10.1007/s12257-015-0733-5>.
- (9) Sokolov, S. V.; Tschulik, K.; Batchelor-McAuley, C.; Jurkschat, K.; Compton, R. G. Reversible or Not? Distinguishing Agglomeration and Aggregation at the Nanoscale. *Analytical Chemistry* **2015**, *87* (19), 10033–10039. <https://doi.org/10.1021/acs.analchem.5b02639>.
- (10) Zhang, W. Nanoparticle Aggregation: Principles and Modeling. In *Nanomaterial*; Capco, D. G., Chen, Y., Eds.; Springer Netherlands: Dordrecht, 2014; Vol. 811, pp 19–43. https://doi.org/10.1007/978-94-017-8739-0_2.
- (11) Berka, M.; Rice, J. A. Relation between Aggregation Kinetics and the Structure of Kaolinite Aggregates. *Langmuir* **2005**, *21* (4), 1223–1229. <https://doi.org/10.1021/la0478853>.
- (12) Sugimoto, T.; Kobayashi, M.; Adachi, Y. The Effect of Double Layer Repulsion on the Rate of Turbulent and Brownian Aggregation: Experimental Consideration. *Colloids and Surfaces A: Physicochemical and Engineering Aspects* **2014**, *443*, 418–424. <https://doi.org/10.1016/j.colsurfa.2013.12.002>.

- (13) Zhang, W.; Yao, Y.; Li, K.; Huang, Y.; Chen, Y. Influence of Dissolved Oxygen on Aggregation Kinetics of Citrate-Coated Silver Nanoparticles. *Environ. Pollut.* **2011**, *159* (12), 3757–3762. <https://doi.org/10.1016/j.envpol.2011.07.013>.
- (14) Ma, R.; Levard, C.; Marinakos, S. M.; Cheng, Y.; Liu, J.; Michel, F. M.; Brown, G. E.; Lowry, G. V. Size-Controlled Dissolution of Organic-Coated Silver Nanoparticles. *Environ. Sci. Technol.* **2012**, *46* (2), 752–759. <https://doi.org/10.1021/es201686j>.
- (15) Choi, O.; Deng, K. K.; Kim, N.-J.; Ross, L.; Surampalli, R. Y.; Hu, Z. The Inhibitory Effects of Silver Nanoparticles, Silver Ions, and Silver Chloride Colloids on Microbial Growth. *Water Research* **2008**, *42* (12), 3066–3074. <https://doi.org/10.1016/j.watres.2008.02.021>.
- (16) Qu, H.; Mudalige, T. K.; Linder, S. W. Capillary Electrophoresis/Inductively-Coupled Plasma-Mass Spectrometry: Development and Optimization of a High Resolution Analytical Tool for the Size-Based Characterization of Nanomaterials in Dietary Supplements. *Analytical Chemistry* **2014**, *86* (23), 11620–11627. <https://doi.org/10.1021/ac5025655>.
- (17) Boer, P. K. M. J. S. T. K. J. de. Asymmetric Flow Field-Flow Fractionation Analysis of Engineered Nanoparticles in Mouthwashes and Their Interaction with Saliva <http://www.chromatographyonline.com/asymmetric-field-flow-fractionation-analysis-engineered-nanoparticles-mouthwashes-and-their-interact> (accessed Oct 7, 2018).
- (18) Mudalige, T. K.; Qu, H.; Van Haute, D.; Ansar, S. M.; Linder, S. W. Capillary Electrophoresis and Asymmetric Flow Field-Flow Fractionation for Size-Based Separation of Engineered Metallic Nanoparticles: A Critical Comparative Review. *TrAC Trends in Analytical Chemistry* **2018**, *106*, 202–212. <https://doi.org/10.1016/j.trac.2018.07.008>.
- (19) Lawler, D. F.; Youn, S.; Zhu, T.; Kim, I.; Lau, B. L. T. Comprehensive Understanding of Nano-Sized Particle Separation Processes Using Nanoparticle Tracking Analysis. *Water Science and Technology* **2015**, *72* (12), 2318–2324. <https://doi.org/10.2166/wst.2015.459>.
- (20) Sharma, R. An Environmental Transmission Electron Microscope for in Situ Synthesis and Characterization of Nanomaterials. *Journal of Materials Research* **2005**, *20* (07), 1695–1707. <https://doi.org/10.1557/JMR.2005.0241>.
- (21) Yoshida, K.; Bright, A. N.; Ward, M. R.; Lari, L.; Zhang, X.; Hiroyama, T.; Boyes, E. D.; Gai, P. L. Dynamic Wet-ETEM Observation of Pt/C Electrode Catalysts in a Moisturized Cathode Atmosphere. *Nanotechnology* **2014**, *25* (42), 425702. <https://doi.org/10.1088/0957-4484/25/42/425702>.
- (22) Shard, A. G.; Sparnacci, K.; Sikora, A.; Wright, L.; Bartczak, D.; Goenaga-Infante, H.; Minelli, C. Measuring the Relative Concentration of Particle Populations Using Differential Centrifugal Sedimentation. *Analytical Methods* **2018**, *10* (22), 2647–2657. <https://doi.org/10.1039/C8AY00491A>.
- (23) Nilsson, M. L. M. U. S. L. Practical Applications of Asymmetrical Flow Field-Flow Fractionation (AF4): A Review http://www.chromatographyonline.com/practical-applications-asymmetrical-flow-field-flow-fractionation-af4-review-0?__hstc=753710.0840654798ac9432210439b9e9a090f1.1546893450664.154689

3450664.1546893450664.1&__hssc=753710.1.1546893450665&__hsfp=646542350 (accessed Jan 7, 2019).

- (24) Dieckmann, Y.; Cölfen, H.; Hofmann, H.; Petri-Fink, A. Particle Size Distribution Measurements of Manganese-Doped ZnS Nanoparticles. *Anal. Chem.* **2009**, *81* (10), 3889–3895. <https://doi.org/10.1021/ac900043y>.
- (25) Murdock, R. C.; Braydich-Stolle, L.; Schrand, A. M.; Schlager, J. J.; Hussain, S. M. Characterization of Nanomaterial Dispersion in Solution Prior to In Vitro Exposure Using Dynamic Light Scattering Technique. *Toxicol Sci* **2008**, *101* (2), 239–253. <https://doi.org/10.1093/toxsci/kfm240>.
- (26) Lodeiro, P.; Achterberg, E. P.; Pampin, J.; Affatati, A.; El-Shahawi, M. S. Silver Nanoparticles Coated with Natural Polysaccharides as Models to Study AgNP Aggregation Kinetics Using UV-Visible Spectrophotometry upon Discharge in Complex Environments. *Science of The Total Environment* **2016**, *539*, 7–16. <https://doi.org/10.1016/j.scitotenv.2015.08.115>.
- (27) Cheng, W.; Compton, R. G. Electrochemical Detection of Nanoparticles by ‘Nano-Impact’ Methods. *TrAC Trends in Analytical Chemistry* **2014**, *58*, 79–89. <https://doi.org/10.1016/j.trac.2014.01.008>.
- (28) Rees, N. V.; Zhou, Y.-G.; Compton, R. G. Making Contact: Charge Transfer during Particle–Electrode Collisions. *RSC Adv.* **2012**, *2* (2), 379–384. <https://doi.org/10.1039/C2RA01100J>.
- (29) Fosdick, S. E.; Anderson, M. J.; Nettleton, E. G.; Crooks, R. M. Correlated Electrochemical and Optical Tracking of Discrete Collision Events. *J. Am. Chem. Soc.* **2013**, *135* (16), 5994–5997. <https://doi.org/10.1021/ja401864k>.
- (30) Ellison, J.; Tschulik, K.; Stuart, E. J. E.; Jurkschat, K.; Omanović, D.; Uhlemann, M.; Crossley, A.; Compton, R. G. Get More Out of Your Data: A New Approach to Agglomeration and Aggregation Studies Using Nanoparticle Impact Experiments. *ChemistryOpen* **2013**, *2* (2), 69–75. <https://doi.org/10.1002/open.201300005>.
- (31) Zeng, S.; Baillargeat, D.; Ho, H.-P.; Yong, K.-T. Nanomaterials Enhanced Surface Plasmon Resonance for Biological and Chemical Sensing Applications. *Chemical Society Reviews* **2014**, *43* (10), 3426. <https://doi.org/10.1039/c3cs60479a>.
- (32) Osman, M. E.; Eid, M. M.; Khatib, O.; Kolthoum, H.; El-Hallouty, S. M.; El-Marakby, S. M.; Mahmoud, D. A. Spectroscopic Characterization of the Effect of Gamma Radiation on the Physical Parameters of Biosynthesized Silver/Chitosan Nano-Particles and Their Antimicrobial Activity. *Materials Research Express* **2015**, *2* (9), 095023. <https://doi.org/10.1088/2053-1591/2/9/095023>.
- (33) nanoComposix. NanoXact Silver Nanospheres – Bare (Citrate) <https://nanocomposix.com/products/nanoxact-silver-nanospheres-bare-citrate> (accessed Jan 7, 2019).
- (34) Loumagne, M.; Midelet, C.; Doussineau, T.; Dugourd, P.; Antoine, R.; Stamboul, M.; Débarre, A.; Werts, M. H. V. Optical Extinction and Scattering Cross Sections of Plasmonic Nanoparticle Dimers in Aqueous Suspension. *Nanoscale* **2016**, *8* (12), 6555–6570. <https://doi.org/10.1039/C6NR00918B>.
- (35) Baalousha, M.; Nur, Y.; Römer, I.; Tejamaya, M.; Lead, J. R. Effect of Monovalent and Divalent Cations, Anions and Fulvic Acid on Aggregation of

- Citrate-Coated Silver Nanoparticles. *Science of The Total Environment* **2013**, 454–455, 119–131. <https://doi.org/10.1016/j.scitotenv.2013.02.093>.
- (36) nanoComposix. BioPure Silver Nanospheres – Bare (Citrate) <https://nanocomposix.com/products/biopure-silver-nanospheres-bare-citrate> (accessed Jan 7, 2019).
- (37) Harris, D. C. *Quantitative Chemical Analysis*, 7th edition.; W. H. Freeman: New York, 2006.
- (38) Zhou, Y.-G.; Haddou, B.; Rees, N. V.; Compton, R. G. The Charge Transfer Kinetics of the Oxidation of Silver and Nickel Nanoparticles via Particle–Electrode Impact Electrochemistry. *Physical Chemistry Chemical Physics* **2012**, 14 (41), 14354. <https://doi.org/10.1039/c2cp42940c>.
- (39) Bartlett, T. R.; Sokolov, S. V.; Compton, R. G. Electrochemical Nanoparticle Sizing Via Nano-Impacts: How Large a Nanoparticle Can Be Measured? *ChemistryOpen* **2015**, 4 (5), 600–605. <https://doi.org/10.1002/open.201500061>.
- (40) Yi, Y.; Weinberg, G.; Prenzel, M.; Greiner, M.; Heumann, S.; Becker, S.; Schlögl, R. Electrochemical Corrosion of a Glassy Carbon Electrode. *Catalysis Today* **2017**, 295, 32–40. <https://doi.org/10.1016/j.cattod.2017.07.013>.
- (41) Honeycomb Spectroelectrochemical Cell. *Pine Research Instrumentation Store*, 2016.
- (42) Chemical Compatability Chart. Thermo Fisher Scientific Inc. 2013.
- (43) Rees, N. V.; Zhou, Y.-G.; Compton, R. G. The Aggregation of Silver Nanoparticles in Aqueous Solution Investigated via Anodic Particle Coulometry. *ChemPhysChem* **2011**, 12 (9), 1645–1647. <https://doi.org/10.1002/cphc.201100207>.
- (44) Xie, R.; Batchelor-McAuley, C.; Young, N. P.; Compton, R. G. Electrochemical Impacts Complement Light Scattering Techniques for *in Situ* Nanoparticle Sizing. *Nanoscale* **2019**, 11 (4), 1720–1727. <https://doi.org/10.1039/C8NR09172B>.
- (45) Help Online - Origin Help - ExpDec1 <https://www.originlab.com/doc/Origin-Help/ExpDec1-FitFunc> (accessed Apr 3, 2019).